Thermal Fatigue Behavior of AISI H13 Hot Work Tool Steel Produced by Direct Laser Metal Deposition

Massimo Pellizzari,* Daniel Massignani, Sasan Amirabdollahian, and Faraz Deirmina

Direct laser metal deposition (DLMD) is an additive manufacturing technique getting growing attention thanks to the possibility of producing very complex parts in a short time and in a cost-effective manner. The possible applications of this technology are tools with conformal cooling channels and claddings for dies and molds reparation. One of the damaging mechanisms of tools is thermal fatigue (TF) cracking, leading to surface deterioration and, consequently, the processed parts. Herein, the TF behavior of DLMD-H13 submitted to two different heat treatments, namely direct tempering (T) and quenching and tempering (QT), is investigated. T does not significantly change the solidification microstructure after DLMD, whereas QT produces a more homogenous tempered martensite microstructure. A customary laboratory test is developed to induce TF damage under a cyclic temperature variation between 630 and 60 °C. The results evidence that the T-H13 has a slightly better TF resistance with respect to QT-H13 due to the higher tempering resistance of T-H13 with respect to QT-H13. Thus, according to TF test results, direct tempering can be preferred to quench and tempering since the elimination of quenching can decrease the costs of production as well as distortions-related issues, increasing the competitiveness of DLMD.

1. Introduction

Direct laser metal deposition (DLMD), also known as direct energy deposition (DED) is an additive manufacturing (AM) technique getting growing attention thanks to the possibility to produce very complex parts in short time and in a cost-effective manner.[1,2] The possible applications of this technology are

tools and dies with conformal cooling channels[3,4] and dies and molds reparation.[5,6]

AISI H13 is a widely used hot work tool steel grade, typically applied for hot forming applications like die-casting, hot forging, and extrusion dies, thanks to its excellent combination of good hardness, high toughness, hot yield strength, and tempering resistance. Conventional manufacturing of parts in this steel involves ingot casting, eventual electroslag/vacuum remelting, thermomechanical processing, one or more mechanical- and/or electro-discharge machining steps, and final high-quality heat treatment.[7,8] Therefore, the cost dedicated to the production of tools and dies is high, representing an important burden for the final cost of products. Thanks to the relatively high toughness and low susceptibility to cold cracking during 3D printing, the use of H13 powders has been also extended to laser powder bed fusion (LPBF) and DLMD processes, with important benefits on the possibility to fabricate large functional parts or prototypes with complex geometries, cladding,[9,10] repair, and in situ combination of materials for producing functionally graded materials.[11] Despite the difficulties in processing H13 by DED, due to residual stress accumulation resulting from martensitic transformation, numerous studies have been conducted in recent years for successful deposition and characterization of L-DED H13 parts for tooling applications.[12,13]

Properties are strongly related to the peculiar microstructure after DLMD, as well as to the post-process heat treatment used. While conventionally processed tool steels undergo austenitization and quenching prior to tempering,[7,8] it has been suggested that AM-H13, experiencing a fast cooling after deposition, the as-built microstructure can be potentially subjected to direct tempering.[14] Deirmina et al.[15] compared the effect of two heat treatment scenarios for LPBF processed H13 and demonstrated that direct tempering provides better static fracture toughness compared with the quenched and tempered counterpart due to the secondary crack formation and crack deflection. The influence of heat treatment on the microstructure of H13 processed by DLMD was also studied by Amirabdollahian.[16,17] The as-built steel is characterized by retained austenite (RA) and carbides on the intercellular/inter-dendritic areas, due to heavy microsegregation of alloying elements. The conventional heat treatment

M. Pellizzari, D. Massignani, S. Amirabdollahian
Department Industrial Engineering
University of Trento
Via Sommarive 9, Trento 38123, Italy
E-mail: massimo.pellizzari@unitn.it

F. Deirmina
Powder R&D
Sandvik Additive Manufacturing
Sandvik Machining Solutions AB
Mossvägen 10, Sandviken 811 82, Sweden

involving austenitization at 1020 °C is not suitable for recovery of the microsegregation and dissolution of carbides. The highest secondary hardness was achieved by direct tempering of the as-built material, and the secondary hardening peak was shifted to a slightly higher temperature compared with quenched counterparts due to the higher amount of RA, the higher dislocation density, and the finer martensite substructure in AB condition. Direct tempering was claimed to be the most effective post-processing heat treatment for DLMD-H13, as far as high strength, hardness, and tempering resistance are the main applications targets. In contrast, the authors warned about the detrimental effect of the interconnected carbide network at prior cellular/dendritic boundaries, particularly with regard to toughness and fatigue resistance.

Thermal fatigue (TF) is an important damaging mechanism of tools, which causes the formation of a crack network (heat checking) and the deterioration of the surface finishing, with important consequences on process costs.[18] The heat checking resistance can be improved by a suitable combination of hot strength, ductility, and toughness together with inherent high thermal conductivity and low coefficient of thermal expansion. The positive influence of the fine grain size on TF resistance under low maximum test temperature (600–700 °C) could be demonstrated. Under limited thermo-mechanical loading conditions, the higher toughness resulting from a finer grain size and microstructure becomes of paramount importance.[19] The positive influence of high tempering resistance on TF cracks nucleation and propagation could be described for wrought hot work tool steels[20,21] as well as for similar grades produced by mechanical milling and spark plasma sintering.[22]

The TF resistance of AM tool steel has been very poorly studied in the literature. Meng compared the TF resistance of SLM-H13 in the as-built condition with that after direct tempering at 500 and 600 °C, and with that to the forged steel grade.[23] The as-built material showed the lowest thermal crack length, whereas the forged steel was the worst. This good behavior of the as-built condition was related to secondary hardening taking place during the test, the dissolution of the cellular solidification substructure, the decomposition of the RA into martensite, and the precipitation of carbides. Indeed, the use of as-built H13 seems to be of poor practical meaning, due to the high brittleness of virgin martensite, the extra thermomechanical stresses associated with the local tempering of martensite and the decomposition of RA during the TF test, and the presence of residual stresses. The behavior of DLMD H13 tool steel coating on copper alloy substrate was described in ref. [24] in which two types of cracks: 1) networks of fine and shallow cracks and 2) large catastrophic cracks were detected.

Tuning of heat treatment to achieve the best suitable microstructure and TF resistance is of paramount importance. In this work, the TF behavior of DLMD H-13 submitted to two different heat treatments, namely direct tempering and quench and tempering, has been investigated. A customary laboratory test was used to evaluate TF damage on a laboratory scale. The total surface crack length, density, and penetration depth were correlated to microstructure and tempering resistance.

2. Materials and Experimental Techniques

A commercial AISI H13 powder for AM by Sandvik Osprey was used for obtaining the samples. Its chemical composition is highlighted in **Table 1** and the particle size distribution was characterized by d10, d50, and d90 values equal to 57, 81, and 109 μm, respectively.

A 5 mm thick H13 cladding has been laser deposited on a mild steel C40 bar with a diameter of 30 mm (**Figure 1**). Direct laser deposition of H13 was performed by a DMG MORI LASERTEC 65 3D hybrid machine equipped with a COAX-14 powder nozzle and a 2500 W diode laser ($\lambda = 1020$ nm). The coaxial nozzle introduced the powder into the melt-pool through argon carrier gas (5 L min^{-1}) and provided a shielding atmosphere around the melt-pool using Argon flow (6 L min^{-1}). Laser spot diameter was set to 3 mm, with a top-hat beam profile and a focal length of 13 mm. A rotary additive helical around-part scanning strategy has been adopted. A laser power of 1200 W, a scanning speed of 1000 mm min^{-1}, and a powder feed rate of 12 g min^{-1} have been used.

Cylindrical samples (40 mm diameter, 20 mm in width) were electro discharge machining cut and ground to a final surface roughness of 0.4 Ra. The samples were heat treated using two different strategies to achieve the same target hardness of 450 HV (a quite common hardness for tool steel dies), using the tempering curves of DED H13 tool steel.[17] The first set of samples (T-H13) was directly double tempered for 2 h at 650 °C and finally slowly cooled to room temperature. The second set of samples quenching and tempering (QT-H13) was austenitized at 1020 °C × 15 min, gas quenched using a 5 bar N$_2$ flow, and finally double tempered at 625 °C for 2 h. Before reaching the austenitizing temperature a preheating stage at 700 °C was introduced to guarantee a thermal homogenization of the samples.

TF tests were conducted on a customary equipment. The sample, mounted on a shaft rotating with an angular velocity (ω) of 4 rpm was induction heated up to 630 °C and later rapidly cooled to 60 °C by a water jet (flow rate = 1.5 cm^3 s^{-1}) impinging the disc surface. To ensure reaching the minimum temperature during each TF cycle, the sample was further immersed in a water box, before starting the following induction heating. The maximum target temperature was measured just after the inductor by means of an infrared pyrometer. The emissivity was set to 0.8, i.e., the emissivity of iron oxide measured by the previous study. The test was periodically interrupted to evaluate TF cracking and the surface microhardness profile. As the heated zone width was about 10, the 20 mm width sample underwent a double thermal gradient, i.e., one along the depth below the surface, and one along the width, between the central zone (heated by the inductor) nd the cold edges of the samples. To remove any limescale deposits, the samples have been washed in a 10% acetic acid solution in an ultrasound washing machine, for 30 min. After that, to prepare the surface for scanning electron microscopy (SEM) analysis and microhardness measurement the surface

Table 1. Nominal composition (in wt%) of the AISI H13 powder.

	C	Cr	Ni	Mn	Mo	V	Si	Fe
H13	0.4	5.2	–	0.5	1.6	1.1	1.0	Bal.
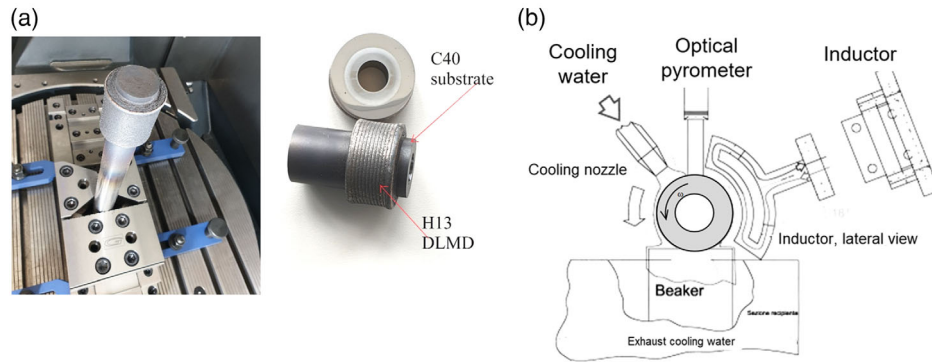
Figure 1. a) Direct laser metal deposition (DLMD)-H13 cladding on a C40 steel bar, with detail of the platform setup used for the deposition process. b) Schematic of thermal fatigue rig.
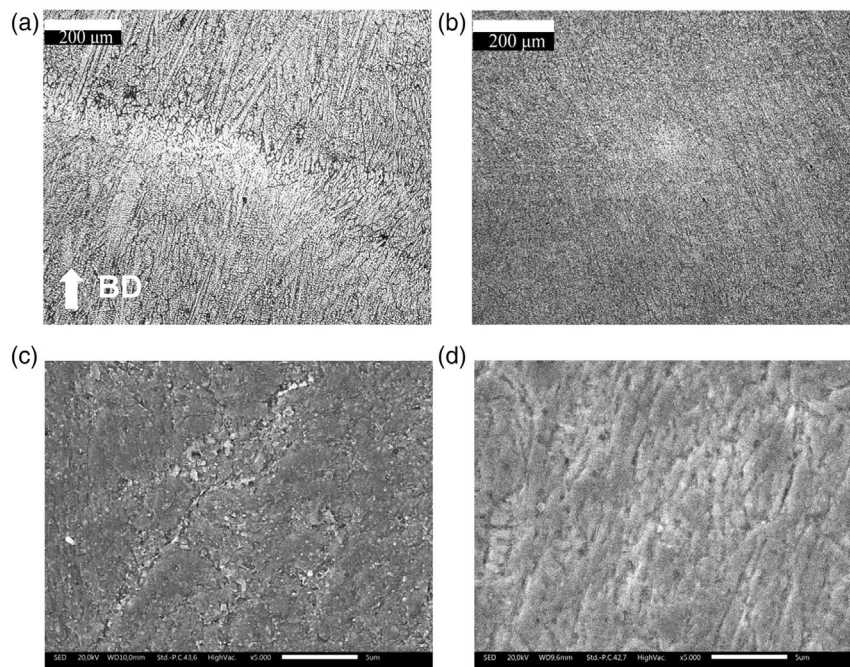
was slightly polished with 3 μm diamond paste, to remove the dark oxide surface layer, and to make the cracks visible by SEM and light optical microscopy. Vickers microhardness measurements have been performed according to ASTM E92-82 using a load of 100 g (HV0.1). The surface microhardness profiles have been measured every 500 cycles along the width of the sample and, at the end of the test, along the depth from the surface, to evaluate the softening caused by the cyclic thermal exposure during TF tests. The data hardness was averaged on three measurements.

Quantitative image analysis of surface TF cracking was carried out at regular test intervals (500, 750, 1000, and 1500 cycles) by Leica Qwin software. The crack density (n°cracks mm^{-2}), the total crack length (mm), and the maximum crack length (mm) were calculated. Moreover, at the end of tests, the samples have been cut to evaluate the crack penetration depth.

3. Results and Discussion

3.1. Microstructural Characterization

Figure 2a shows the microstructure of T-H13 after Nital etching. After the double tempering treatment at 650 °C without prior quench treatment, the melt pool boundaries and the solidification microstructure are still evident. At melt pool boundaries, in which the solidification rate is very rapid, a cellular microstructure is formed, whereas in the rest of the melting pool the structure is mainly dendritic/columnar. A preferential growth direction of the dendrites is observed normal to the solidification front. An average layer thickness of 0.83 ± 0.03 mm was measured. The tempered martensite microstructure of QT-H13 (Figure 2b) is far more homogeneous than that of T-13, without any more traces of prior solidification structure. It can be concluded that

Figure 2. Microstructure of DLMD: a) T-H13 (OM), b) QT-H13 (OM), c) T-H13 (SEM), and d) QT-H13 (SEM).

2200449 (3 of 7)

**ADVANCED
SCIENCE NEWS**

www.advancedsciencenews.com

**steel
research**
international

www.steel-research.de

austenitizing at 1020 °C, promoting the formation of new austenite grains, largely deletes the melt pool boundaries as well as the columnar structure typically observed in the as-built material.[16,17]

In Figure 2c, higher magnification SEM micrographs of T-H13 clearly show a strong submicrometric precipitation of carbides at the prior cell boundary, forming an almost interconnected network, as well as the precipitation of carbides inside the cell. The preferential precipitation at cell boundaries is related to the local decomposition of RA during tempering.[17] In AB-H13, RA is mostly present at cell boundaries, due to the local enrichment in alloying elements caused by microsegregation, stabilizing austenite down to room temperature. The bigger carbides, isolated with respect to the interconnected network of finer carbides, are plausibly proeutectoid carbides that precipitate during the solidification at a much higher temperature with respect to that of tempering, in which the atomic diffusion is typically high. Figure 2d evidences no visible precipitates in QT-H13, as a result of finer and more homogeneous precipitation taking place after quenching. In fact, it was demonstrated that RA is completely removed after quenching. In spite of the different treatment cycles used to achieve the same target hardness, the hardness of QT-H13 and T-H13 was 500 and 455 HV, respectively, possibly due to some temperature nonuniformity inside the vacuum furnace during QT treatment.
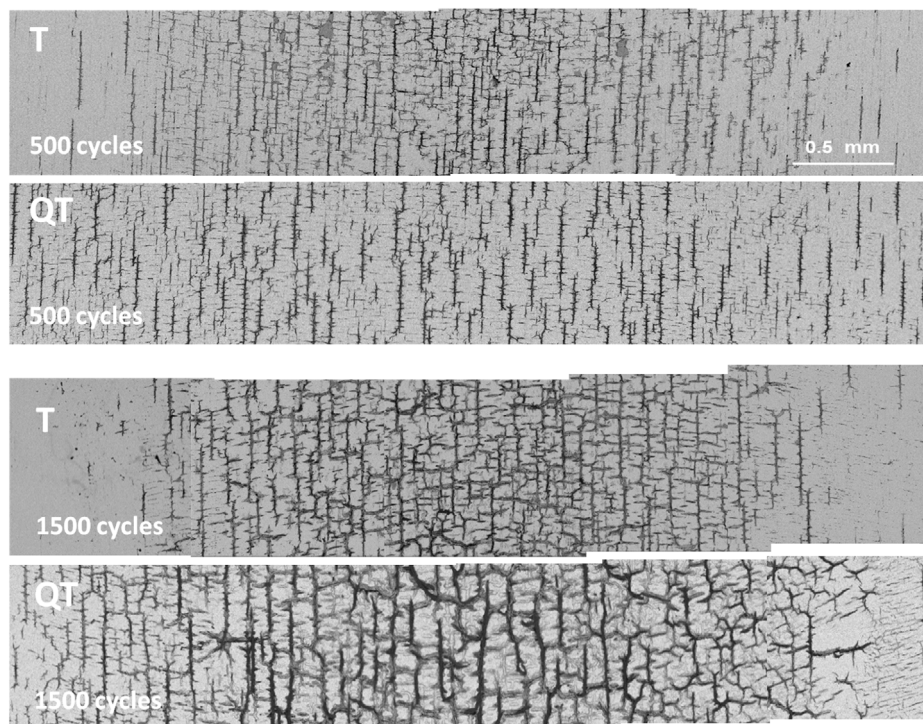
3.2. Thermal Cracking

Figure 3 shows a general view of the surface damage after 500 and 1500 cycles for T-H13 and QT-H13 samples, respectively. From these micrographs, it is possible to qualitatively evaluate the evolution of TF cracking. For both samples, after 500 cycles

cracking is predominant along the revolution direction (RD), with only limited short cracks along the transversal direction (TD). A closer view highlights that transversal cracks preferentially nucleate from the longitudinal ones, which were already present. The crack length increases by increasing the number of cycles, in particular along the RD, becoming progressively more and more interconnected.
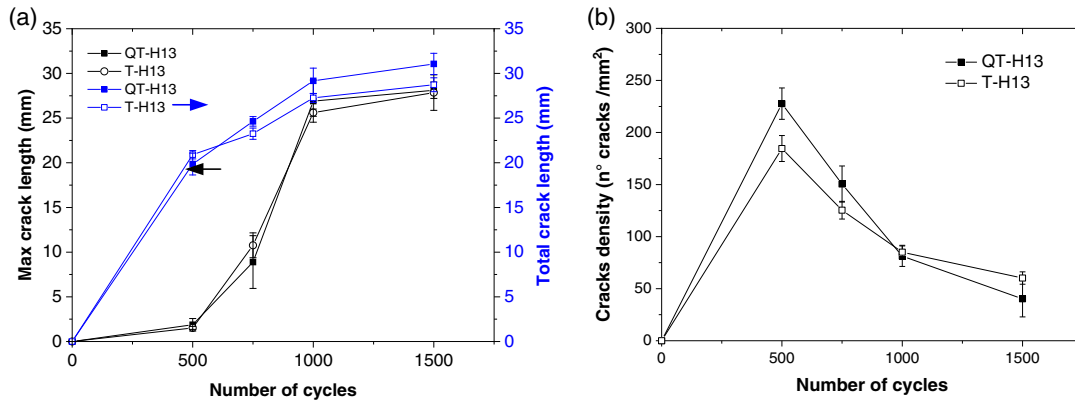
A quantitative evaluation of cracking is reported in **Figure 4**: the total crack length (Figure 4a) increases quite rapidly during the first 500 cycles, during which more than 50% of propagation takes place. The crack propagation rate measured considering the total crack length becomes lower during the rest of the test, particularly during the last 500 cycles in which it is practically negligible. The maximum crack length increases more slowly, with a sharp increase between 500 and 1000 cycles. In the last TF period, it approaches the total crack length, as the result of the progressive crack interconnection shown by micrographs. This effect is clearly confirmed in Figure 4b, in which the negative slope of the crack density curve after the first 500 cycles highlights the interconnection of existing growing cracks.

The maximum crack penetration depth, measured on two metallographic cross sections, parallel and normal to the RD, slightly exceeds 0.1 mm, whereas the average depth is less than 50 μm (**Table 2**). In general, the results in Figure 4 and Table 2 confirm that the TF resistance of DLMD-H13 is only poorly affected by the specific heat treatment condition: directly tempered T-H13 shows almost the same behavior of QT-H13 and even better, as far as the total crack length and the crack depth on the circumferential section are considered.

This seems to suggest that the worse microstructure of T-H13 (Figure 2) does not practically affect the resistance to

Figure 3. Surface damage of T-H13 and QT-H13 after 500 and 1500 TF cycles. (↑RD, ↔TD).

ADVANCED
SCIENCE NEWS
www.advancedsciencenews.com

steel
research
international
www.steel-research.de

Figure 4. TF damage: a) crack length and b) crack density evolution for QT-H13 and T-H13.

Table 2. Average and maximum crack depth for the QT and T.

Average depth cracks [μm]	QT	T
Radial section	37 μm	35 μm
Circumferential section	42 μm	35 μm
Max depth cracks [μm]	QT	T
Radial section	105 μm	107 μm
Circumferential section	134 μm	108 μm

thermal cracking. Any possible detrimental influence of the solidification microstructure and of the interconnected carbide network in T-H13 could be also excluded by fracture toughness measurements, showing that, at a similar hardness level (500 HV), QT parts showed just higher K_{app} (89 MPa$\sqrt{m}$) than DT (70 MPa $\sqrt{m}$).[17] Anyway, the fracture toughness values obtained for both parts were comparable with that of wrought H13. Therefore, the relatively good TF resistance of T-H13 has to be justified by looking at other intrinsic properties such as tempering resistance.
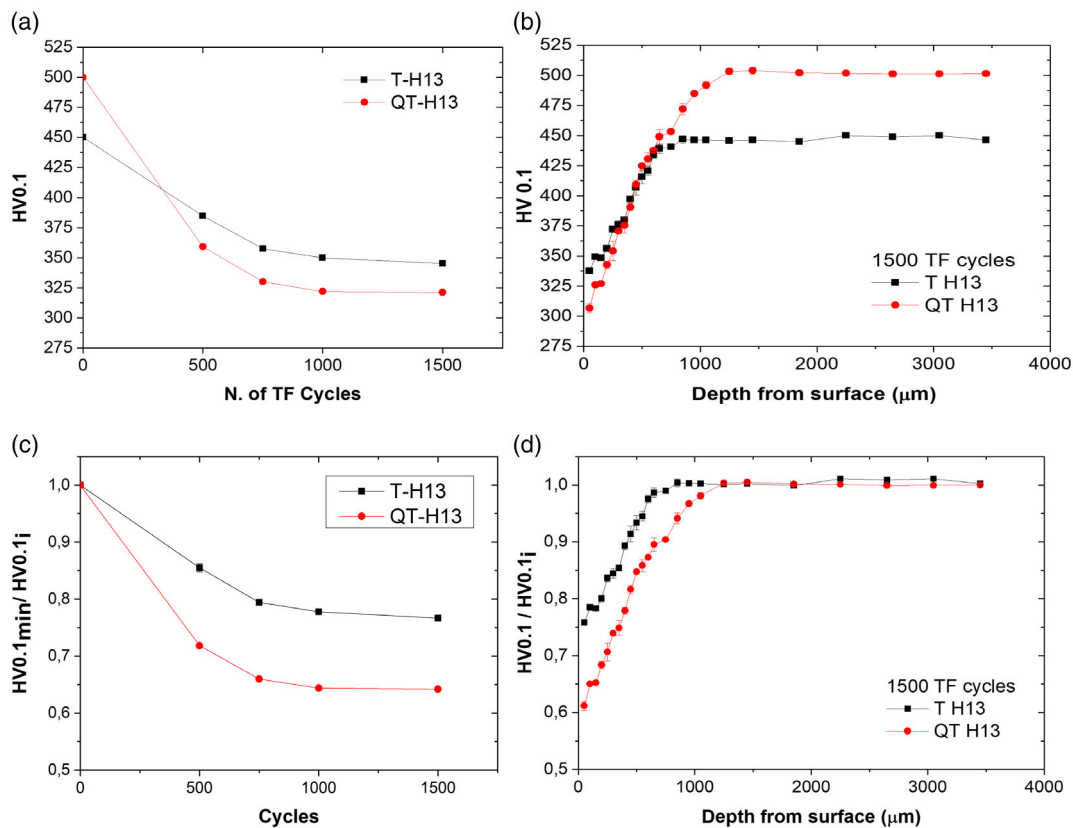
Figure 5. Thermal softening was measured: a) on the surface after different TF cycles and b) below the surface of T-H13 and QT-H13. c,d) report the same curves normalized over the initial hardness HV0.1$_i$ of the samples.

3.3. Thermal Softening

Figure 5a displays the minimum surface hardness measured in the central region of the TF disc, which experienced the maximum temperature during the test. In the light of the different starting hardness of T-H13 and QT-H13, in Figure 5c thermal softening is also reported as the drop in normalized hardness (the actual hardness, H, divided by the starting hardness Hi). In both cases, most of the softening is accumulated during the first 500 cycles, during which most of the TF damage was also accumulated (see Figure 4). Further softening is very limited during the rest of the test, as observed for crack length. This correlation between TF cracking and tempering resistance was observed in previous papers, also by present authors.[20] The tempering resistance of T-H13 is higher than that of QT-H13: while the final hardness of T-H13 is about 80% of the starting one, that of QT-H13 approached 65%. Of course, the difference must be partially attributed to the lower tempering temperature of QT-H13 (625 °C) than T-H13 (650 °C), especially considering that the maximum temperature during the TF test is 630 °C. In contrast, the higher tempering resistance of T-H13 could be more clearly demonstrated by isothermal annealing at 600 and 650 °C up to 40 h for two T-H13 and QT-H13 samples with the same initial hardness of 520 HV, obtained after tempering at 600 and 650 °C, respectively.[17] These results confirm that the finer microstructure after DLMD, better preserved after direct tempering than after QT, plays a positive role in tempering resistance: in particular, the high dislocations density introduced by rapid solidification creates more nucleation sites for carbide precipitation and decreased carbide growth time.[25]

To further remark the higher tempering resistance of T-H13 than QT-H13, the microhardness profiles after 1500 cycles below the surface are reported in Figure 5b,d. Both, the softening depth and drop in hardness are lower for T-H13. Comparing the maximum crack depths in Table 2, it is also evident that all cracks are inside the thermally softened region, confirming that thermal softening plays an important role with respect to both, crack nucleation and propagation. In this respect, the peculiar behavior of T-H13 and QT-H13 will need to be further investigated.

4. Conclusion

The TF resistance of H13 tool steel produced by DLMD was studied. Two different heat treatment conditions were considered, namely direct tempering of as-built material (T-H13) and QT (QT-H13). T-H13 shows a finer but quite inhomogeneous microstructure, with clear traces of prior cellular/dendritic structure and preferential secondary carbide precipitation at cell boundary. The microstructure of QT-H13 consists of a tempered martensite strengthened by very fine and homogeneously dispersed secondary carbides. TF cracking (heat checking) is poorly affected by the different microstructures: in particular, T-H13 is characterized by slightly lower surface crack length and lower penetration depth than QT-H13. This result could be ascribed to the higher tempering resistance of T-H13 and supports the possible use of direct tempering in place of more expensive QT for tooling applications.

Conflict of Interest

The authors declare no conflict of interest.

Data Availability Statement

Research data are not shared.

[1] S. M. Thompson, L. Bian, N. Shamsaei, A. Yadollahi, *Addit. Manuf.* **2015**, *8*, 36.

[2] D. Svetlizky, M. Das, B. Zheng, A. L. Vyatskikh, S. Bose, A. Bandyopadhyay, J. M. Schoenung, E. J. Lavernia, N. Eliaz, *Mater. Today* **2021**, *49*, 271.

[3] M. Cortina, J. I. Arrizubieta, A. Calleja, A. Alberdi, *Metals* **2018**, *8*, 102.

[4] M. B. Mawale, *Rapid Prototyp. J.* **2018**, *24/8*, 1347.

[5] M. Perini, P. Bosetti, N. Balc, *Rapid Prototyp. J.* **2020**, *26/5*, 929.

[6] A. J. Pinkerton, W. Wang, L. Li, *Proc. Inst. Mech. Eng. B: J. Eng. Manuf.* **2008**, *222*, 827.

[7] *ASM Specialty Handbook: Tool Materials*, (Ed: J. R. Davis), ASM International, Carlsbad, CA p. 1995.

[8] G. A. Roberts, R. Kennedy, G. Krauss, *Tool Steels*, 5th ed, ASM International, Materials Park, OH **1998**.

[9] M. K. Imran, S. H. Masood, M. Brandt, *Lasers Manufact. Mater. Process.* **2015**, *2*, 242.

[10] Z. Zhao, M. Perini, P. Bosetti, M. Pellizzari, presented at *12th Tooling Conf. and Exhibition*, Őrebro, Sweden, April 2022.

[11] H. Mei, J. Ouyang, D. Hu, R. Kovacevic, in *22nd Int. Congress on Laser Materials Processing and Laser Microfabrication* **2003**, p. 903.

[12] N. S. Bailey, C. Katinas, Y. C. Shin, *J. Mater. Process. Tech.* **2017**, *247*, 223.

[13] J. Mazumder, J. Choi, K. Nagarathnam, J. Koch, D. Hetzner, *J. Mater.* **1997**, *49*, 55.

[14] J. Krell, A. Röttger, K. Geenen, W. Theisen, *J. Mater. Process. Technol.* **2018**, *255*, 679.

[15] F. Deirmina, N. Peghini, B. AlMangour, D. Grzesiak, M. Pellizzari, *Mater. Sci. Eng. A* **2019**, *753*, 109.

[16] S. Amirabdollahian, F. Deirmina, M. Pellizzari, P. Bosetti, A. Molinari, *Mater. Sci. Eng. A* **2021**, *814*, 141126.

[17] S. Amirabdollahian, F. Deirmina, M. Benedetti, P. Bosetti, M. Pellizzari, A. Molinari, presented at *12th Tooling Conf. and Exhibition*, Őrebro, Sweden, April 2022.

[18] M. Pellizzari, A. Molinari, *Mater. Manuf. Process.* **2009**, *24*, 723.

[19] J. Sjöström, J. Bergström, *J. Mater. Process. Technol.* **2004**, *153–154*, 1089.

[20] M. Pellizzari, A. Molinari, D. Cescato, A. Ghidini, S. Cantini, *Int. J. Microstruct. Mater. Properties* **2008**, *3*, 363.

**ADVANCED
SCIENCE NEWS**

www.advancedsciencenews.com

**steel
research**
international

www.steel-research.de

[21] A. Persson, S. Hogmark, J. Bergström, *Int. J. Fatigue* **2004**, *26*, 1095.

[22] F. Deirmina, M. Pellizzari, *Proc. of TOOL 2016, ASMET*, Bratislava, Slovakia, June 2016.

[23] C. Meng, C. Wu, X. Wang, J. Li, R. Cao, *Metals* **2019**, *9*, 773.

[24] M. Khalid Imran, S. H. Masood, M. Brandt, S. Bhattacharya, S. Gulizia, M. Jahedi, J. Mazumder, *Surf. Coat. Technol.* **2012**, *206*, 2572.

[25] D. C. Saha, E. Biro, A. P. Gerlich, Y. Zhou, *Mater. Character.* **2020**, *168*, 110564.